ACADEMIC PRESS

Available online at www.sciencedirect.com

SCIENCE DIRECT®

Journal of Computational Physics 187 (2003) 1–21

JOURNAL OF COMPUTATIONAL PHYSICS

www.elsevier.com/locate/jcp

Numerical approach to simulating turbulent flow of a viscoelastic polymer solution

T. Vaithianathan, Lance R. Collins *

Department of Chemical Engineering, The Pennsylvania State University, University Park 16802, USA
Sibley School of Mechanical and Aerospace Engineering, Cornell University, Ithaca, NY 14853-7501, USA

Received 29 April 2002; received in revised form 16 October 2002; accepted 21 December 2002

Abstract

In this paper, we present two new numerical algorithms for updating the equations of motion for a viscoelastic fluid that can be described by the finite extensible nonlinear elastic polymer model with the closure proposed by Peterlin (so called FENE-P model) in a transient calculation. In particular, our algorithms address two difficulties found in earlier formulations. First, the polymer extension, represented by the trace of the conformation tensor, can numerically exceed the finite extensible length causing the restoring spring force to change sign and the calculation to rapidly diverge. In our formulations, we have redefined the conformation tensor so that this possibility no longer exists. Secondly, the conformation tensor must remain symmetric and positive definite at all times for the calculation to remain stable. The accumulation of numerical errors can cause loss of this property, leading to the growth of Hadamard instabilities [J. Non-Newtonian Fluid Mech. 60 (1995) 53]. We present two matrix decompositions that enable us to construct the conformational tensor in a manner that ensures positive definiteness. Numerical tests of the new algorithms show significant departures from other approaches that rely on filtering to remove the instabilities.

PACS: 65N12; 76A10; 76F05

Keywords: Turbulence; Direct numerical simulations; Non-Newtonian; Viscoelastic; FENE; FENE-P

1. Introduction

Numerical simulation of viscoelastic flows of dilute polymer solutions has benefited from a new class of constitutive models known as finite extensible nonlinear elastic (FENE) models. These models are based on a molecular, coarse-grained treatment of the polymer molecule as a collection of beads and springs. Beads represent blocks of monomer that are small enough that their rotational motion is highly correlated—the characteristic length being defined as a Kuhn length [1]. The springs account for the tendency of the

* Corresponding author.
E-mail address: LC246@cornell.edu (L.R. Collins).

0021-9991/03/$ - see front matter
doi:10.1016/S0021-9991(03)00028-7

polymer chain to assume configurations that leave the molecule in a ball. The spring should be viewed as a probabilistic (or entropic) spring that restores a stretched molecule into configurations that are more probable. Traditional Hookean springs lead to a class of models known as Oldroyd B fluids. This approximation is reasonable for weakly stretched polymer molecules, but is unphysical for polymer molecules undergoing large strains.

In contrast, FENE models have been shown to reproduce many properties found experimentally [2,3]. Moreover, these models have a stronger statistical mechanical foundation that enables physical properties in the model to be more easily estimated for a specific polymer–solvent combination [4]. However, the FENE model is still not a closed constitutive model that can be embedded into a fluid mechanics code. Closure for the two-bead dumbbell has been postulated by Peterlin [5], resulting in a model that is generally referred to as the FENE-P model. The FENE-P model requires solution of an orientation tensor, $C_{ij} \equiv \langle r_i r_j \rangle$, which describes the average orientation of the polymer chains at each point in the fluid, where r_i is the separation vector between the two beads. The polymer contribution to the stress tensor is then related nonlinearly to the orientation tensor.

Early attempts to embed the FENE-P model in a direct numerical simulation of turbulent flow for the purpose of studying drag reduction were plagued by numerical difficulties [6]. Sureshkumar and Beris [7] traced the problem to the numerical update of the conformation tensor and introduced an artifical stress diffusivity into the equation to damp the growth of Hadamard instabilities. This lead to a series of successful numerical simulations of turbulent drag reduction by Beris and coworkers [8–11] and others [12–15]. Despite the success of the approach, there remains the question of how much the artificial stress diffusivity is masking or otherwise modifying the physics of the fluctuating polymer stresses, particularly at high wavenumbers, where presumably the damping will be strongest.

In light of this earlier work, we can identify three distinct issues associated with simulating a turbulent flow field with the FENE-P model. First, the finite extensibility of the polymer manifests in the model as a limit for the trace of the conformation tensor. Unfortunately, numerical errors, particularly in the vicinity of a strongly extensional flow, can lead to predictions for the polymer extension that exceed the bound, causing the restoring force to change sign and the simulation to rapidly diverge. This can be partially alleviated by solving the equations implicitly; however, iterations that encounter this problem will dramatically slow the rate of convergence. The second problem is associated with the eigenvalues of C_{ij}, which should remain positive. Negative eigenvalues are equivalent to locally negative viscosities, which cause the unbounded growth of instabilities in the flow. The third issue is not, strictly speaking, a numerical problem, but is associated with the current formulation of the FENE-P model. Because the equation for the conformation tensor contains no diffusion term (or other dissipation mechanism), turbulence (or any 'mixing' flow [16] for that matter) will generate sharp gradients (shocks) in the conformation tensor. This causes the stress divergence to increase, possibly without bound, with increasing grid resolution. Physically we expect some molecular mechanism to truncate this process; however, the nature of that truncation is not clear; moreover, the argument for the molecular cutoff should come from *modeling* not numerical considerations (at least initially).

We propose two entirely new formulations based on decompositions of the conformation tensor that address the numerical problems discussed above. The approach is similar to the one used by [17] to evaluate integrals of the conformation tensor; however, in this instance we use the decomposition to guarantee positivity of all of the eigenvalues of the conformation tensor independent of the strength of the flow. By eliminating the possibility of instabilities due to negative eigenvalues, we are able to more clearly expose the issue of the resolution of the conformation tensor (in the absence of a molecular diffusion term). The paper is organized as follows. We begin with a brief summary of the basic governing equations in Section 2. This is followed by a detailed description of the two new formulations of the FENE-P model in Sections 3 and 4. We show results of both numerical algorithms in Section 5 followed by conclusions in Section 6.

2. Governing equations

We are interested in solving the equations of motion for forced and decaying isotropic turbulence in a periodic cube of length 2π along each dimension. Below we summarize the equations that govern a uniform, dilute polymer solution in an incompressible solvent whose stress is described by the FENE-P model.

2.1. Velocity field

The fluid is assumed to be an incompressible continuum, and so it satisfies a generalized form of the Navier Stokes equations

$$\nabla \cdot \mathbf{u} = 0, \tag{1}$$

$$\frac{\mathrm{D}\mathbf{u}}{\mathrm{D}t} \equiv \frac{\partial \mathbf{u}}{\partial t} + \mathbf{u} \cdot \nabla \mathbf{u} = -\frac{1}{\rho}\nabla p + \frac{1}{\rho}\nabla \cdot \mathbf{T} + \mathbf{a}_{\mathrm{F}}(\mathbf{x}, t), \tag{2}$$

where $\mathbf{u}(\mathbf{x}, t)$ is the velocity vector, ρ is the fluid density, $p(\mathbf{x}, t)$ is the local pressure, $\mathbf{T}$ is the the combination of the viscous and polymer stresses and $\mathbf{a}_{\mathrm{F}}(\mathbf{x}, t)$ is an external forcing function that is used (in some simulations) to generate a stationary turbulent field. The forcing is added in spectral space to wavenumbers in the range $0 \leqslant k \leqslant \sqrt{2}$ using a vector-valued, incompressible Ornstein–Ulenbeck process with a prescribed variance and decay rate that is fixed for all of the forced simulations (see [18] for a detailed discussion of forcing). The mass concentration of polymer is assumed to be uniform in space and time and dilute, so its effect on the other properties of the solvent can be neglected.

Note the following about our nomenclature. First, as shown in Eq. (2), we hereafter will use $\mathrm{D}/\mathrm{D}t$ to refer to the material (substantial) derivative. All vectors will be designated by a bold lower case letter and all tensors will be designated by a bold upper case letter. On the occasions that we use indicial notation, we will refer to the variable by the same letter with standard text and appropriate subscripts.

The stress tensor can be written as a linear sum of contributions from the Newtonian solvent and the polymer as follows:

$$\mathbf{T} \equiv \mathbf{T}^{[\mathrm{s}]} + \mathbf{T}^{[\mathrm{p}]}, \tag{3}$$

where $\mathbf{T}^{[\mathrm{s}]}$ is the Newtonian stress from the solvent defined as

$$\mathbf{T}^{[\mathrm{s}]} = 2\mu^{[0]}\beta \boldsymbol{S}, \tag{4}$$

$\beta \equiv \mu/\mu^{[0]}$ is the ratio of the solvent viscosity to the solution viscosity at zero shear, $\boldsymbol{S} \equiv (\nabla \mathbf{u} + \nabla \mathbf{u}^{\mathrm{T}})/2$ is the rate of strain tensor and $\mathbf{T}^{[\mathrm{p}]}$ is the polymer stress, discussed in greater detail below (see Section 2.2). The parameter β is proportional to the polymer concentration; for example, if we assume the zero-stress configuration of the polymer is small spheres, then at dilute concentrations the polymer viscosity scales like $\mu^{[\mathrm{p}]} = \mu\phi$, where ϕ is the polymer volumetric concentration—under this circumstance, $(1 - \beta) = \phi/(1 + \phi) \approx \phi$ in the dilute limit.

2.2. Constitutive model for the polymer

The FENE-P model has a number of features that make it suitable for describing a dilute solution of polymer molecules. In particular, finite extensibility makes the viscometric response of the polymer more agreeable with experimental observations [19]. In the FENE-P model, the polymer stress is defined as

$$\mathbf{T}^{[p]} = \mu^{[0]}(1-\beta)\frac{f(r)\mathbf{C}-\mathbf{I}}{\tau_p}, \tag{5}$$

where $\mathbf{C}$ is the conformation tensor, discussed in greater detail below, $r^2 \equiv \mathrm{Tr}(\mathbf{C})$ is the square of the mean separation between the beads, $\mathbf{I}$ is the identity tensor, and τ_p is the Zimm relaxation time of the polymer. The function $f(r)$ is the so-called Peterlin function defined as

$$f(r) = \frac{L^2-3}{L^2-r^2}, \tag{6}$$

where L is the maximum extension of the polymer. This function gives rise to a nonlinear spring force that diverges as $r \to L$, ensuring the spring cannot extend beyond L. At this stage, the polymer stress is expressed entirely in terms of the conformation tensor, $\mathbf{C}$, which satisfies

$$\frac{\mathrm{D}\mathbf{C}}{\mathrm{D}t} = \mathbf{C}\cdot\nabla\mathbf{u} + \nabla\mathbf{u}^{\mathrm{T}}\cdot\mathbf{C} - \frac{f(r)\mathbf{C}-\mathbf{I}}{\tau_p}. \tag{7}$$

2.3. Properties of the conformation tensor

The conformation tensor, $\mathbf{C}$, is a measure of the second-order moment of the end-to-end distance vector of the polymer dumbbell. It can be written as [20]

$$C_{ij} \equiv \langle r_i r_j \rangle, \tag{8}$$

where the vector $\mathbf{r}$ is the separation vector between the two beads of the dumbbell. From the definition, it follows that the conformation tensor is a symmetric positive definite (SPD) matrix. [1] Hulsen [21] proved that during exact time evolution the conformation tensor must remain positive definite if it were initially. However, cumulative numerical errors that arise from virtually all initial value problem algorithms can give rise to negative eigenvalues. The presence of negative eigenvalues causes the unbounded growth of Hadamard instabilities that quickly overwhelm the calculation [7].

Another important property of the conformation tensor is that the trace, which represents the square of the separation distance, must always be less than the square of the maximum extension, i.e., $r^2 \leqslant L^2$. The model guarantees this property through the force term, which diverges in strength as this limit is approached. Hence for flows of arbitrary strength, the restoring force is always sufficient to maintain this constraint. However, numerical errors in the evaluation of $\mathrm{Tr}(\mathbf{C})$ can lead to violations of this constraint. Extension past L^2 causes the force to change sign, resulting in the rapid divergence of the calculation.

2.4. Parameters

The addition of the polymer stress to the momentum balance introduces several new parameters. Here, we summarize all of the dimensionless parameters required to completely specify an isotropic simulation. Recall that for isotropic, Newtonian turbulence, the fluid motion is characterized by the Reynolds number; here we define an analogous Reynolds number based on the solution viscosity and the Taylor microscale

[1] A symmetric matrix $\mathbf{A}$ is said to be SPD if $\mathbf{y}^{\mathrm{T}}\cdot\mathbf{A}\cdot\mathbf{y} > 0$ for arbitrary $\mathbf{y}$. As the conformation tensor is a variance–covariance matrix, the Cauchy–Schwartz inequality guarantees that it is non-negative definite. Moreover, the additional constraint $\langle r_i r_i \rangle > 0$ makes the conformation tensor a SPD.

$$Re \equiv \sqrt{15}\frac{U'^2}{\sqrt{\nu^{[0]}\epsilon}}, \tag{9}$$

where U' is the turbulence intensity, ϵ is the rate of dissipation of turbulence, and $\nu^{[0]} \equiv \mu^{[0]}/\rho$ is the solution kinematic viscosity at zero shear. In addition, we have the parameter β, which represents the polymer concentration. The polymer maximum extension L is a dimensionless parameter normalized by the equilibrium extension. Finally, the polymer relaxation time can be used to define a non-dimensional Weissenberg number

$$We \equiv \frac{\tau_p}{\tau_\eta} = \frac{\tau_p}{\sqrt{\nu^{[0]}/\epsilon}}, \tag{10}$$

where τ_η is the Kolmogorov time scale associated with the smallest eddies. Weissenberg numbers that are significant as compared to unity are required in order to see an appreciable effect of the polymer.

3. Continuous eigendecomposition

A symmetric, positive-definite matrix such as $\mathbf{C}$ can be expressed in terms of its eigenvalues and eigenvectors as follows:

$$\mathbf{C} = \mathbf{U}\boldsymbol{\Lambda}\mathbf{U}^{\mathrm{T}}, \tag{11}$$

where $\boldsymbol{\Lambda}$ is a diagonal matrix made up of the three eigenvalues of $\mathbf{C}$, λ_1, λ_2 and λ_3, $\mathbf{U} = [\mathbf{u}_1, \mathbf{u}_2, \mathbf{u}_3]$ is a matrix whose columns are the unit eigenvectors of $\mathbf{C}$, $\mathbf{u}_1$, $\mathbf{u}_2$ and $\mathbf{u}_3$ and $\mathbf{U}^{\mathrm{T}}$ is the transpose of $\mathbf{U}$. Note that since the eigenvectors of $\mathbf{C}$ are orthogonal, we immediately obtain $\mathbf{U}\mathbf{U}^{\mathrm{T}} = \mathbf{I}$. By updating the matrices $\boldsymbol{\Lambda}$ and $\mathbf{U}$ and constructing $\mathbf{C}$ using Eq. (11), we guarantee positive definiteness of the matrix $\mathbf{C}$, so long as the individual eigenvalues remain greater than zero. This requirement can be more easily enforced by the numerical algorithm.

3.1. Evolution equations for $\boldsymbol{U}$ and $\boldsymbol{\Lambda}$

To take advantage of Eq. (11), we must derive evolution equations for $\mathbf{U}(t)$ and $\boldsymbol{\Lambda}(t)$. We begin by rewriting the equation for $\mathbf{C}$ as

$$\frac{\mathrm{D}\mathbf{C}}{\mathrm{D}t} = \mathbf{C}\mathbf{S} + \mathbf{S}\mathbf{C} + \mathbf{C}\mathbf{R} - \mathbf{R}\mathbf{C} - \frac{f(r)\mathbf{C} - \mathbf{I}}{\tau_p},$$

in terms of the rate of strain and rate of rotation tensors, defined, respectively, as:

$$\mathbf{S} \equiv \left(\nabla\mathbf{u} + \nabla\mathbf{u}^{\mathrm{T}}\right)/2,$$

$$\mathbf{R} \equiv \left(\nabla\mathbf{u} - \nabla\mathbf{u}^{\mathrm{T}}\right)/2,$$

where $\mathbf{S}$ is a symmetric tensor and $\mathbf{R}$ is skew symmetric (antisymmetric). From the orthogonality properties of $\mathbf{U}$ we can say $\boldsymbol{\Lambda} = \mathbf{U}^{\mathrm{T}}\mathbf{C}\mathbf{U}$. Differentiating using the chain rule yields

$$\begin{aligned}\frac{\mathrm{D}\boldsymbol{\Lambda}}{\mathrm{D}t} &= \frac{\mathrm{D}\mathbf{U}^{\mathrm{T}}}{\mathrm{D}t}\mathbf{C}\mathbf{U} + \mathbf{U}^{\mathrm{T}}\frac{\mathrm{D}\mathbf{C}}{\mathrm{D}t}\mathbf{U} + \mathbf{U}^{\mathrm{T}}\mathbf{C}\frac{\mathrm{D}\mathbf{U}}{\mathrm{D}t} \\ &= \frac{\mathrm{D}\mathbf{U}^{\mathrm{T}}}{\mathrm{D}t}\mathbf{U}\boldsymbol{\Lambda} + \mathbf{U}^{\mathrm{T}}\left[\mathbf{C}\mathbf{S} + \mathbf{S}\mathbf{C} + \mathbf{C}\mathbf{R} - \mathbf{R}\mathbf{C} - \frac{f(r)\mathbf{C} - \mathbf{I}}{\tau_p}\right]\mathbf{U} + \boldsymbol{\Lambda}\mathbf{U}^{\mathrm{T}}\frac{\mathrm{D}\mathbf{U}}{\mathrm{D}t}.\end{aligned}$$

Next we define

$$\mathbf{H} \equiv \mathbf{U}^{\mathrm{T}} \frac{\mathrm{D}\mathbf{U}}{\mathrm{D}t}, \tag{12}$$

and note that after integrating by parts we have

$$\mathbf{H} = \frac{\mathrm{D}\mathbf{U}^{\mathrm{T}}\mathbf{U}}{\mathrm{D}t} - \frac{\mathrm{D}\mathbf{U}^{\mathrm{T}}}{\mathrm{D}t}\mathbf{U} = -\frac{\mathrm{D}\mathbf{U}^{\mathrm{T}}}{\mathrm{D}t}\mathbf{U} = -\mathbf{H}^{\mathrm{T}},$$

which implies that $\mathbf{H}$ is skew symmetric. Substituting this above and eliminating $\mathbf{C}$ yields

$$\frac{\mathrm{D}\mathbf{\Lambda}}{\mathrm{D}t} = -\mathbf{H}\mathbf{\Lambda} + \mathbf{\Lambda}(\mathbf{B}+\mathbf{D}) + (\mathbf{B}-\mathbf{D})\mathbf{\Lambda} - \frac{f(r)\mathbf{\Lambda}-\mathbf{I}}{\tau_{\mathrm{p}}} + \mathbf{\Lambda}\mathbf{H}, \tag{13}$$

where

$$\mathbf{B} \equiv \mathbf{U}^{\mathrm{T}}\mathbf{S}\mathbf{U}, \tag{14}$$

$$\mathbf{D} \equiv \mathbf{U}^{\mathrm{T}}\mathbf{R}\mathbf{U}. \tag{15}$$

The diagonal elements of the terms involving $\mathbf{H}$ and $\mathbf{R}$ are all identically zero, and therefore cannot contribute to the time evolution of $\mathbf{\Lambda}(t)$. We therefore can split Eq. (13) into two simpler expressions representing the diagonal and off-diagonal terms, respectively:

$$\begin{cases} \dfrac{\mathrm{D}\lambda_i}{\mathrm{D}t} = 2B_{ii}\lambda_i - \dfrac{f(r)\lambda_i - 1}{\tau_{\mathrm{p}}}, & i = j, \\ 0 = [\mathbf{\Lambda}(\mathbf{B}+\mathbf{D}+\mathbf{H}) + (\mathbf{B}-\mathbf{D}-\mathbf{H})\mathbf{\Lambda}]_{ij}, & i \neq j. \end{cases} \tag{16}$$

The top expression in Eq. (16) is the evolution equation for the eigenvalues of $\mathbf{C}$; the lower part can be used to solve for the tensor $\mathbf{H}$ as shown below

$$H_{ij} = \begin{cases} \dfrac{[\mathbf{\Lambda}(\mathbf{B}+\mathbf{D}) + (\mathbf{B}-\mathbf{D})\mathbf{\Lambda}]_{ij}}{\lambda_j - \lambda_i}, & i \neq j, \\ 0, & i = j. \end{cases} \tag{17}$$

Finally, we need to derive an evolution equation for the tensor $\mathbf{U}$. To update $\mathbf{U}$ we can take advantage of definition of $\mathbf{H}$ and the fact that $\mathbf{U}$ is an orthogonal matrix to obtain

$$\frac{\mathrm{D}\mathbf{U}}{\mathrm{D}t} = \mathbf{U}\mathbf{H}. \tag{18}$$

3.2. Numerical algorithm

As noted in [14,15], advection of the conformation tensor is complicated by the lack of a diffusion term. As will be shown, this leads to the formation of steep gradients in $\mathbf{C}$ (and therefore $\mathbf{T}^{[\mathrm{p}]}$), as would occur for a passive scalar for example [22]. A pseudospectral algorithm has difficulties dealing with the steep gradients [14,15]; moreover, the standard dealiasing step [23,24], which involves zeroing a portion of the wavenumber space, will corrupt the eigenvalues. We therefore use a compact finite difference scheme to update $\mathbf{U}$ and $\mathbf{\Lambda}$ [25]. The velocity is updated using a standard pseudospectral code [26]; details can be found elsewhere [27].

The algorithm for updating the conformation tensor and fluid velocity proceeds as follows. Given $\mathbf{U}_n$, $\mathbf{\Lambda}_n$, $\mathbf{u}_n$, where the subscript n indicates the iteration number

1. Update $\mathbf{U}_{n+1}$
2. Update $\mathbf{\Lambda}_{n+1}$
3. Construct
   - $\mathbf{C}_{n+1} \equiv \mathbf{U}_{n+1}\mathbf{\Lambda}_{n+1}\mathbf{U}_{n+1}^{\mathrm{T}}$
   - $\mathbf{T}_{n+1}^{[p]}$ from Eq. (5)
   - $\mathbf{T}_{n+1} \equiv \mathbf{T}_{n+1}^{[s]} + \mathbf{T}_{n+1}^{[p]}$
4. Update $\mathbf{u}_{n+1}$

The details for accomplishing the first two steps is given below.

3.2.1. Numerical update of U

The convective equation for $\mathbf{U}$ is

$$\frac{\partial \mathbf{U}}{\partial t} + \mathbf{u}\cdot\nabla\mathbf{U} = \mathbf{U}\mathbf{H}, \tag{19}$$

which can be rewritten as follows:

$$\frac{\partial \mathbf{U}}{\partial t} = \mathbf{U}\mathscr{H}, \tag{20}$$

where

$$\mathscr{H} \equiv \mathbf{H} - \mathbf{U}^{\mathrm{T}}[\mathbf{u}\cdot\nabla\mathbf{U}].$$

Note that by definition $\mathbf{U}^{\mathrm{T}}[\mathbf{u}\cdot\nabla\mathbf{U}]$ is skew symmetric (and therefore so is $\mathscr{H}$). It is critical that the numerical update of $\mathbf{U}$ maintain its orthogonality.

The traditional explicit Euler update of Eq. (20) takes the form

$$\begin{aligned}\mathbf{U}_{n+1} &= \mathbf{U}_n[\mathbf{I} + h\mathscr{H}_n] + \mathrm{O}(h^2) = \mathbf{U}_0[\mathbf{I} + h\mathscr{H}_0][\mathbf{I} + h\mathscr{H}_1]\cdots[\mathbf{I} + h\mathscr{H}_n] + \mathrm{O}(h^2)\\ &= \mathbf{U}_0\left[\mathbf{I} + h\sum_{i=0}^{n}\mathscr{H}_i\right] + \mathrm{O}(h^2),\end{aligned} \tag{21}$$

where h is the time step. However, this update does not guarantee that $\mathbf{U}_{n+1}$ remains an orthogonal matrix. A symplectic integrator guarantees orthogonality. For example, a modified version of the Euler scheme based on the Cayley expansion [28] can be written as shown below

$$\mathbf{U}_{n+1} = \mathbf{U}_0\left[\mathbf{I} - \frac{h}{2}\sum_{i=0}^{n}\mathscr{H}_i\right]^{-1}\left[\mathbf{I} + \frac{h}{2}\sum_{i=0}^{n}\mathscr{H}_i\right] + \mathrm{O}(h^2). \tag{22}$$

Eq. (22) is equivalent to Eq. (21) to $\mathrm{O}(h^2)$; however, its form guarantees that $\mathbf{U}_{n+1}$ remains orthogonal. Note that we typically set $\mathbf{U}_0 = \mathbf{I}$, eliminating that pre-factor. Additionally, we use an analytical expression for the product shown in Eq. (22). For a skew symmetric matrix $\mathbf{A}$

$$\mathbf{A} \equiv \begin{bmatrix} 0 & -c & b \\ c & 0 & -a \\ -b & a & 0 \end{bmatrix},$$

$(\mathbf{I}-\mathbf{A})^{-1}(\mathbf{I}+\mathbf{A})$ is given by

$$\frac{1}{(1+a^2+b^2+c^2)}\begin{bmatrix} 1+a^2-b^2-c^2 & 2(ab+c) & 2(ac-b) \\ 2(ab-c) & 1-a^2+b^2-c^2 & 2(bc+a) \\ 2(ac+b) & 2(bc-a) & 1-a^2-b^2+c^2 \end{bmatrix}.$$

3.2.2. Numerical update of Λ

The upper expression in Eq. (16) shows the governing equation for the eigenvalues. An important consideration in designing a numerical update for this equation is that the eigenvalues must satisfy the constraint $\sum_{i=0}^{3}\lambda_i = r^2 \leqslant L^2$. To accomplish this, we treat the nonlinear elastic restoring force implicitly, while the rest of the equation is evaluated explicitly for numerical convenience. Using an integrating factor for the linear terms, the resulting semi-implicit Euler step takes the following form:

$$\lambda_{1[n+1]} = \lambda_{1[n]}e^{2hB_{11}} - h\mathbf{u}_n\cdot\nabla\lambda_{1[n]} + \frac{h}{\tau_p} - \frac{hf(r_{n+1})\lambda_{1[n+1]}}{\tau_p}, \tag{23}$$

$$\lambda_{2[n+1]} = \lambda_{2[n]}e^{2hB_{22}} - h\mathbf{u}_n\cdot\nabla\lambda_{2[n]} + \frac{h}{\tau_p} - \frac{hf(r_{n+1})\lambda_{2[n+1]}}{\tau_p}, \tag{24}$$

$$\lambda_{3[n+1]} = \lambda_{3[n]}e^{2hB_{33}} - h\mathbf{u}_n\cdot\nabla\lambda_{3[n]} + \frac{h}{\tau_p} - \frac{hf(r_{n+1})\lambda_{3[n+1]}}{\tau_p}, \tag{25}$$

where $\lambda_{1[n+1]} \equiv \lambda_1(t_{n+1})$. Next we sum Eqs. (23)–(25) to obtain

$$r_{n+1}^2 = \lambda_{1[n]}e^{2hB_{11}} + \lambda_{2[n]}e^{2hB_{22}} + \lambda_{3[n]}e^{2hB_{33}} - h\mathbf{u}_n\cdot\nabla r_n^2 + \frac{3h}{\tau_p} - \frac{hf(r_{n+1})r_{n+1}^2}{\tau_p}, \tag{26}$$

which can be written in the form

$$r_{n+1}^2 = \gamma - \frac{\alpha r_{n+1}^2}{L^2 - r_{n+1}^2}, \tag{27}$$

where

$$\alpha \equiv \frac{h(L^2-3)}{\tau_p},$$

$$\gamma \equiv \lambda_{1[n]}e^{2hB_{11}} + \lambda_{2[n]}e^{2hB_{22}} + \lambda_{3[n]}e^{2hB_{33}} - h\mathbf{u}_n\cdot\nabla r_n^2 + \frac{3h}{\tau_p}.$$

Eq. (27) is quadratic in r_{n+1}^2 with the following (physical) solution:

$$r_{n+1}^2 = \frac{1}{2}\left[\gamma+\alpha+L^2 - \sqrt{(\gamma+\alpha+L^2)^2 - 4\gamma L^2}\right]. \tag{28}$$

Note that for arbitrarily strong flows (i.e., $\gamma\to\infty$) $0 \leqslant r_{n+1}^2 \leqslant L^2$ is guaranteed. Once computed, r_{n+1}^2 can be substituted into Eqs. (23)–(25) and the eigenvalues $\lambda_{1[n+1]}$, $\lambda_{2[n+1]}$ and $\lambda_{3[n+1]}$ can be updated. Occasionally the numerical update of $\lambda_{i[n+1]}$ go negative. To avoid Hadamard instabilities, we set those eigenvalues to zero and re-normalize the remaining eigenvalues so that the total length is still given by Eq. (28). We can reduce the number of occurrences of negative eigenvalues by reducing the time step h; however, compar-

isons of calculations with smaller time steps show little difference with the results we obtain by this algorithm using the standard Newtonian time step.

3.3. Memory requirements

It is important to consider the memory requirements for this update. Directly integrating the equation for $\mathbf{C}$ requires storage of six independent components of the symmetric tensor. Based on a naive count of variables, it would appear that the eigendecomposition update requires twice as much memory, since three eigenvalues and the nine components of the tensor $\mathbf{U}$ must be stored. However rather than store $\mathbf{U}$, we store globally the skew symmetric tensor $\mathscr{H}(\mathbf{U})$, which has only three independent components, and reconstruct $\mathbf{U}$ (locally) from Eq. (22). Combining these three components with the three eigenvalues yields a total of six global variables, making the memory requirements for the continuous eigendecomposition the same as for direct integration.

4. Cholesky decomposition

An alternative approach to an eigendecomposition of a SPD is a Cholesky decomposition. In this case, we first address the finite extensibility problem by defining a new tensor $\mathbf{J}$ as follows:

$$\mathbf{J} \equiv f(r)\mathbf{C}. \tag{29}$$

Notice that by definition $\mathbf{J}$ is also SPD since $f(r)$ is a positive quantity for all values of r. Taking the trace of both sides of Eq. (29) and rearranging to solve for r^2 in terms of $j^2 \equiv \mathrm{Tr}(\mathbf{J})$ yields

$$r^2 = \frac{j^2 L^2}{L^2 + j^2 - 3}. \tag{30}$$

Notice that $0 \leqslant r^2 \leqslant L^2$ for $0 \leqslant j^2 \leqslant \infty$. Consequently, the finite-extensibility constraint is satisfied as long as we ensure $j^2 > 0$.

From the constitutive equation for $\mathbf{C}$, it is possible to derive the following exact equation for $\mathbf{J}$:

$$\frac{\mathrm{D}\mathbf{J}}{\mathrm{D}t} = \mathbf{J}\cdot\nabla\mathbf{u} + \nabla\mathbf{u}^{\mathrm{T}}\cdot\mathbf{J} - p(\mathbf{J}-\mathbf{I}) + q\mathbf{J}, \tag{31}$$

where

$$\begin{aligned} p &\equiv \frac{L^2 - 3 + j^2}{\tau_{\mathrm{p}} L^2}, \\ q &\equiv \left[\frac{k}{L^2-3} - \frac{(L^2-3+j^2)(j-3)}{\tau_{\mathrm{p}} L^2 (L^2-3)}\right], \\ k &\equiv \mathrm{Tr}[\mathbf{J}\cdot\nabla\mathbf{u} + \nabla\mathbf{u}^{\mathrm{T}}\cdot\mathbf{J}]. \end{aligned} \tag{32}$$

The remaining numerical problem is how to maintain the positive definiteness of the tensor $\mathbf{J}$. The Cholesky decomposition of $\mathbf{J}$ can be expressed as follows:

$$\mathbf{J} = \mathbf{L}\cdot\mathbf{L}^{\mathrm{T}}, \tag{33}$$

where $\mathbf{L}$ is a lower triangular matrix of the form

$$\mathbf{L} \equiv \begin{bmatrix} \ell_{11} & 0 & 0 \\ \ell_{21} & \ell_{22} & 0 \\ \ell_{31} & \ell_{32} & \ell_{33} \end{bmatrix}. \tag{34}$$

If one derives a transport equation for the tensor **L**, and then calculates **J** using Eq. (33), the eigenvalues of **J** will remain positive definite by construction.

4.1. Evolution equations for **L**

Substituting Eq. (34) into Eq. (33) we find

$$\mathbf{J} \equiv \begin{bmatrix} \ell_{11}^2 & \ell_{11}\ell_{21} & \ell_{11}\ell_{31} \\ \ell_{11}\ell_{21} & \ell_{21}^2+\ell_{22}^2 & \ell_{21}\ell_{31}+\ell_{22}\ell_{32} \\ \ell_{11}\ell_{31} & \ell_{21}\ell_{31}+\ell_{22}\ell_{32} & \ell_{31}^2+\ell_{32}^2+\ell_{33}^2 \end{bmatrix}. \tag{35}$$

Notice the tensor is symmetric and the diagonal terms are all positive definite. The equations for the six non-zero elements of the **L** matrix can be derived from the equations for the elements of **J** tensor sequentially, starting with $\ell_{11} = \sqrt{J_{11}}$ and proceeding to ℓ_{21}, ℓ_{31}, ℓ_{22}, ℓ_{32} and finally ℓ_{33}. The result is:

$$\frac{\mathrm{D}\ell_{11}}{\mathrm{D}t} = \Gamma_{11}\ell_{11} + \Gamma_{21}\ell_{21} + \Gamma_{31}\ell_{31} + \frac{1}{2}\left[\frac{p}{\ell_{11}} + (q-p)\ell_{11}\right], \tag{36}$$

$$\frac{\mathrm{D}\ell_{21}}{\mathrm{D}t} = \Gamma_{12}\ell_{11} + \Gamma_{22}\ell_{21} + \Gamma_{32}\ell_{31} + \Gamma_{21}\frac{\ell_{22}^2}{\ell_{11}} + \Gamma_{31}\frac{\ell_{32}\ell_{22}}{\ell_{11}} + \frac{1}{2}\left[-p\ell_{21} - \frac{p\ell_{21}}{\ell_{11}^2} + q\ell_{21}\right], \tag{37}$$

$$\frac{\mathrm{D}\ell_{31}}{\mathrm{D}t} = \Gamma_{13}\ell_{11} + \Gamma_{23}\ell_{21} + \Gamma_{33}\ell_{31} + \Gamma_{21}\frac{\ell_{22}\ell_{32}}{\ell_{11}} + \Gamma_{31}\frac{\ell_{32}^2+\ell_{33}^2}{\ell_{11}} + \frac{1}{2}\left[-p\ell_{31} - \frac{p\ell_{31}}{\ell_{11}^2} + q\ell_{31}\right], \tag{38}$$

$$\frac{\mathrm{D}\ell_{22}}{\mathrm{D}t} = \Gamma_{22}\ell_{22} + \Gamma_{32}\ell_{32} - \Gamma_{21}\frac{\ell_{21}\ell_{22}}{\ell_{11}} - \Gamma_{31}\frac{\ell_{32}\ell_{21}}{\ell_{11}} + \frac{1}{2}\left[-p\ell_{22} + \frac{p}{\ell_{22}} + \frac{p\ell_{21}^2}{\ell_{11}^2\ell_{22}} + q\ell_{22}\right], \tag{39}$$

$$\begin{aligned}\frac{\mathrm{D}\ell_{32}}{\mathrm{D}t} &= \Gamma_{23}\ell_{22} + \Gamma_{33}\ell_{32} - \Gamma_{21}\frac{\ell_{22}\ell_{31}}{\ell_{11}} - \Gamma_{31}\frac{\ell_{31}\ell_{32}}{\ell_{11}} + \Gamma_{32}\frac{\ell_{33}^2}{\ell_{22}} - \Gamma_{31}\frac{\ell_{21}\ell_{33}^2}{\ell_{11}\ell_{22}} \\ &\quad + \frac{1}{2}\left[-p\ell_{32} - \frac{p\ell_{32}}{\ell_{11}^2} - \frac{p\ell_{21}^2\ell_{32}}{\ell_{11}^2\ell_{22}^2} + \frac{p\ell_{21}\ell_{31}}{\ell_{11}^2\ell_{22}} + q\ell_{32}\right],\end{aligned} \tag{40}$$

$$\begin{aligned}\frac{\mathrm{D}\ell_{33}}{\mathrm{D}t} &= \Gamma_{33}\ell_{33} - \Gamma_{31}\frac{\ell_{31}\ell_{33}}{\ell_{11}} - \Gamma_{32}\frac{\ell_{32}\ell_{33}}{\ell_{22}} + \Gamma_{31}\frac{\ell_{21}\ell_{32}\ell_{33}}{\ell_{11}\ell_{22}} - \frac{p\ell_{21}\ell_{31}\ell_{32}}{\ell_{11}^2\ell_{22}\ell_{33}} \\ &\quad + \frac{1}{2}\left[-p\ell_{33} + \frac{p}{\ell_{33}} + \frac{p\ell_{31}^2}{\ell_{11}^2\ell_{33}} + \frac{p\ell_{32}^2}{\ell_{22}^2\ell_{33}} + \frac{p\ell_{21}^2\ell_{32}^2}{\ell_{11}^2\ell_{22}^2\ell_{33}} + q\ell_{33}\right],\end{aligned} \tag{41}$$

J will remain SPD as along as the diagonal elements of **L** are greater than zero.

4.2. Numerical update of **L**

An important consideration for the numerical algorithm used to update the diagonal terms is that they must remain greater than zero. There are a number of numerical approaches to solving for positive definite variables. One that we have used successfully in earlier work is based on a logarithmic transformation as follows [29]:

$$\tilde{\ell}_{11} \equiv \ln(\ell_{11}). \tag{42}$$

The definitions for $\tilde{\ell}_{22}$ and $\tilde{\ell}_{33}$ follow by analogy. Computing ℓ_{11} numerically by exponentiating $\tilde{\ell}_{11}$ yields a positive definite result. The equations for $\tilde{\ell}_{11}$, $\tilde{\ell}_{22}$ and $\tilde{\ell}_{33}$ are found by dividing Eqs. (36), (39) and (41) by ℓ_{11}, ℓ_{22} and ℓ_{33}, respectively. The result is

$$\frac{\mathrm{D}\tilde{\ell}_{11}}{\mathrm{D}t} = \Gamma_{11} + (\Gamma_{21}\ell_{21} + \Gamma_{31}\ell_{31})\exp(-\tilde{\ell}_{11}) + \frac{1}{2}\left[p\exp(-2\tilde{\ell}_{11}) + q - p\right], \tag{43}$$

$$\begin{aligned}\frac{\mathrm{D}\tilde{\ell}_{22}}{\mathrm{D}t} &= \Gamma_{22} + \Gamma_{32}\ell_{32}\exp(-\tilde{\ell}_{22}) - \Gamma_{21}\ell_{21}\exp(-\tilde{\ell}_{11}) - \Gamma_{31}\ell_{32}\ell_{21}\exp(-\tilde{\ell}_{11} - \tilde{\ell}_{22}) \\ &\quad + \frac{1}{2}\left[p\exp(-2\tilde{\ell}_{22}) + p\ell_{21}^2\exp[-2(\tilde{\ell}_{11} + \tilde{\ell}_{22})] + q - p\right],\end{aligned} \tag{44}$$

$$\begin{aligned}\frac{\mathrm{D}\tilde{\ell}_{33}}{\mathrm{D}t} &= \Gamma_{33} - \Gamma_{31}\ell_{31}\exp(-\tilde{\ell}_{11}) - \Gamma_{32}\ell_{32}\exp(-\tilde{\ell}_{22}) + \Gamma_{31}\ell_{21}\ell_{32}\exp(-\tilde{\ell}_{11} - \tilde{\ell}_{22}) \\ &\quad - p\ell_{21}\ell_{31}\ell_{32}\exp(-2\tilde{\ell}_{11} - \tilde{\ell}_{22} - 2\tilde{\ell}_{33}) + \frac{1}{2}\left[p\exp(-2\tilde{\ell}_{33}) + p\ell_{31}^2\exp[-2(\tilde{\ell}_{11} + \tilde{\ell}_{33})]\right. \\ &\quad \left. + p\ell_{32}^2\exp[-2(\tilde{\ell}_{22} + \tilde{\ell}_{33})] + p\ell_{21}^2\ell_{32}^2\exp[-2(\tilde{\ell}_{11} + \tilde{\ell}_{22} + \tilde{\ell}_{33})] + q - p\right].\end{aligned} \tag{45}$$

The numerical algorithm begins by updating $\tilde{\ell}_{11[n+1]}$, $\tilde{\ell}_{22[n+1]}$, $\tilde{\ell}_{33[n+1]}$ and obtains $\ell_{11[n+1]}$, $\ell_{22[n+1]}$ and $\ell_{33[n+1]}$ by exponentiation. We used a standard discretization of the equations for $\tilde{\ell}_{11}$, $\tilde{\ell}_{22}$, $\tilde{\ell}_{33}$, based on a compact finite difference formulation for spatial derivatives and second-order Runge–Kutta for the integration in time. The functions $\ell_{21[n+1]}$, $\ell_{31[n+1]}$ and $\ell_{32[n+1]}$ are then found using Eqs. (37), (38) and (40), respectively. Positivity of the diagonal terms is guaranteed by the logarithmic transformation; positive definiteness of $\mathbf{J}$ is guaranteed by construction. We again used a compact finite difference algorithm (instead of a pseudo-spectral algorithm) to avoid problems resulting from the dealiasing step. The velocity was updated using a standard pseudospectral algorithm.

4.3. Memory requirements

The memory requirements for this update are essentially the same as for the continuous eigendecomposition. The six global variables that must be stored consist of $\tilde{\ell}_{11}$, $\tilde{\ell}_{22}$, $\tilde{\ell}_{33}$, ℓ_{12}, ℓ_{13} and ℓ_{23}. The stress tensor $\mathbf{T}$ can be constructed locally at each grid point without additional storage.

5. Results and discussion

Direct numerical simulations of isotropic, non-Newtonian, turbulent flow were performed on a 64^3 lattice using the algorithms described in Sections 3 and 4. In addition, a limited number of numerical simulations of Eq. (7) were done directly, with the addition of a stress diffusivity of the form $\kappa\nabla^2\mathbf{C}$ on the right-hand side. The additional term introduced a new parameter κ, the stress diffusivity, which we express in terms of a dimensionless Schmidt number defined as

$$Sc \equiv \frac{\nu^{[0]}}{\kappa}. \tag{46}$$

The standard FENE-P model corresponds to $Sc = \infty$, and typical values used in the literature are $Sc \approx 1.0$ [11,12]. The results of all of the simulations are presented below.

5.1. Comparison of numerical algorithms

We integrated the FENE-P model using the continuous eigendecomposition, the Cholesky decomposition and directly integrated Eq. (7) with $Sc = \infty$ and $Sc = 1$. In all cases we set $We = 10$ and $L = 100$, and to facilitate the comparison, we set $\beta = 1$ (i.e., uncoupled) so that we did not have to consider instabilities that might arise from negative eigenvalues. A comparison of the probability density function (PDF) of the polymer stretch r^2/L^2 is given in Fig. 1. There are two problems with the direct integration that are immediately apparent. First, a significant fraction of the points have negative r^2, which is physically unrealistic and if the calculation were fully coupled would lead to numerical instabilities in the velocity field. Note that decreasing the Schmidt number to unity reduces the frequency of occurrence of negative values, but does not eliminate them entirely. The second problem is that the distribution of r^2 on the positive side is greatly attenuated as compared to the continuous eigendecomposition or Cholesky decomposition. In the case of $Sc = 1$, this is due in part to the smoothing of the high frequency eddies by the stress diffusivity. The attenuation at $Sc = \infty$ is most likely due to the moderately large population of negative r^2 which through transport by convection is limiting the growth of the positive values.

In all cases, the continuous eigendecomposition and the Cholesky decomposition maintain $0 \leqslant r^2 \leqslant L^2$. Notice that the resulting distributions are significantly broader than the results from direct integration. It appears as though the two decompositions eliminate the spurious negative values of r^2 without excessive filtering of the dynamics. However, the two methods do not yield identical PDFs. We believe this is due to the numerical difference in the way convection is treated by the two methods. As already noted, convection in this simulation is problematic because of the lack of a molecular mechanism to cut off the unbounded growth of gradients of **C**. As a result, the steep gradients that do arise are presumably truncated by numerical diffusion, which is both grid and method dependent. We observe the discrepancy between the two decompositions only after the steep gradients in **C** are generated and so the underlying cause is undoubtedly

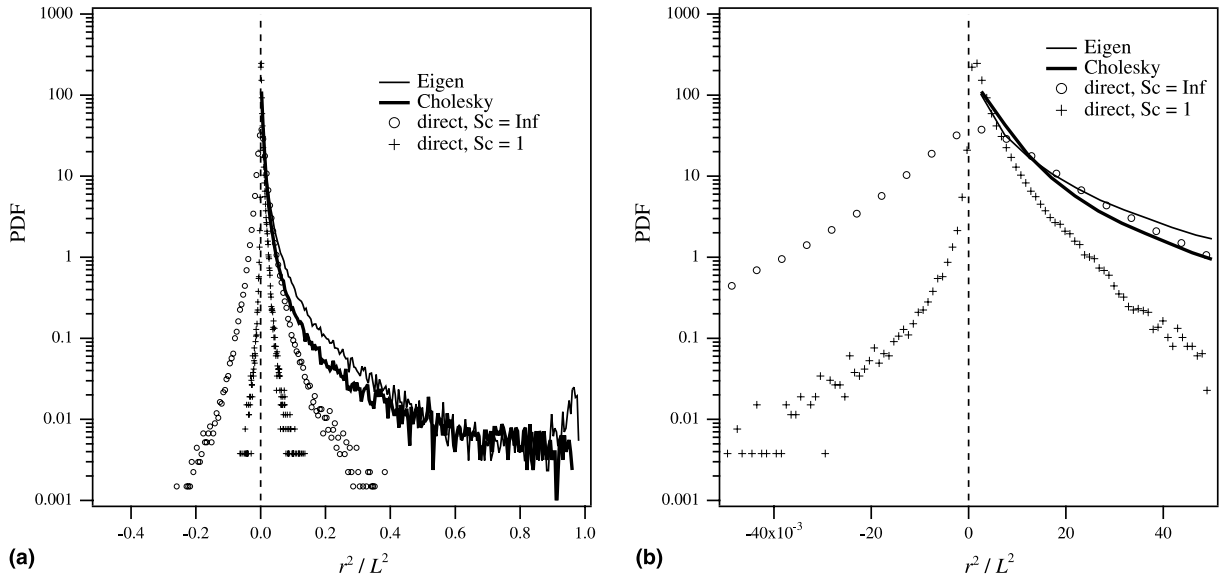

Fig. 1. (a) Comparison of the probability density function (PDF) of the trace of **C** normalized by L^2 for the continuous eigendecomposition method, the Cholesky method, and the direct integration of Eq. (7) with the tensor diffusivity term at the indicated values of Schmidt number. (b) Blow up of the behavior at small r^2/L^2. The parameters for all of the simulations are the same as for Run 2 in Table 1 except $\beta = 1$ (i.e., uncoupled only).

connected to the loss of resolution of the convection terms at long times. Resolution is an important issue that we discuss at greater length in Section 5.4.

5.2. Forced simulations

A series of simulations with large scale forcing (see Eq. (2)) were performed using the continuous eigendecomposition method. Table 1 has a summary of the parameters used in the simulations. We are only showing results for one method because there was general agreement between the two decompositions and the continuous eigendecomposition is the faster of the two. Furthermore, the continuous eigendecomposition required no change in the time step, whereas the Cholesky decomposition required a reduction of the time step by a factor of 5. In each simulation, the polymer was initially unstretched, corresponding to $\mathbf{C} = \mathbf{I}$; however, the simulations were carried out for sufficient time for the polymer stretching to reach steady (stationary) state (approximately six large eddy turnover times) before statistics were calculated. At that point we began statistically sampling at one large eddy turnover time intervals for 20 samples. Averages were computed from these 20 samples.

The effect of Weissenberg number can be seen in Runs 0–3. The turbulence intensities, summarized in the final column of Table 1, are only weakly affected by the polymer until the very highest value ($We = 100$), where the intensity *decreased* by only about 3%. Some of the forcing energy is diverted to maintaining the population of stretched polymer molecules, which slightly reduces the energy available for the turbulent fluctuations. Fig. 2(a) shows the PDF of the trace of the conformation tensor normalized by L^2. We see that the peak in the curve shifts towards the right with increasing Weissenberg number, corresponding to an increase in the degree of stretching. Because the stretching (in this coordinate) cannot exceed unity, we also see a commensurate decrease in the width of the distribution with increasing Weissenberg number leading to a "piling up" of the distribution near unity. At high Weissenberg numbers, a significant fraction of the polymer is being stretched nearly to full extension.

The effect of the maximum extension L on the turbulence can be seen by comparing Runs 0, 1, 4 and 5 in Table 1. We see a similar trend as was seen with the Weissenberg number study; namely that the effect of the polymer is strongest at the highest value of L. Indeed, there is no effect until $L = 1000$, but the effect at this last value is relatively strong, causing the turbulence intensity to drop by 10%. We note that effective drag reducing polymers can have values of L that range from several tens to several hundreds. The effect of L on the PDF of r^2/L^2 is shown in Fig. 2(b). Here the trend is contrary to the Weissenberg number; that is, increases in L cause the polymer to stretch to a smaller fraction of its maximum extension. We believe this is caused by the increase in mechanical energy required to stretch polymers with larger L to the same degree

Table 1
Parameter values used in the forced numerical simulations

Run	β	L^2	We	$(1-\beta)L^2$	U'
0*	1.00	–	–	0	0.833
1	0.95	10^4	1	500	0.833
2*	0.95	10^4	10	500	0.833
3*	0.95	10^4	100	500	0.805
4	0.95	100	10	5	0.833
5*	0.95	10^6	10	5×10^4	0.749
6	0.90	50	10	5	0.833
7	0.90	5×10^3	10	500	0.836
8	0.90	5×10^5	10	5×10^4	0.745

The column labeled U' shows the steady (stationary) state turbulence intensity. Runs with asterisks indicate conditions that decaying studies were also done.

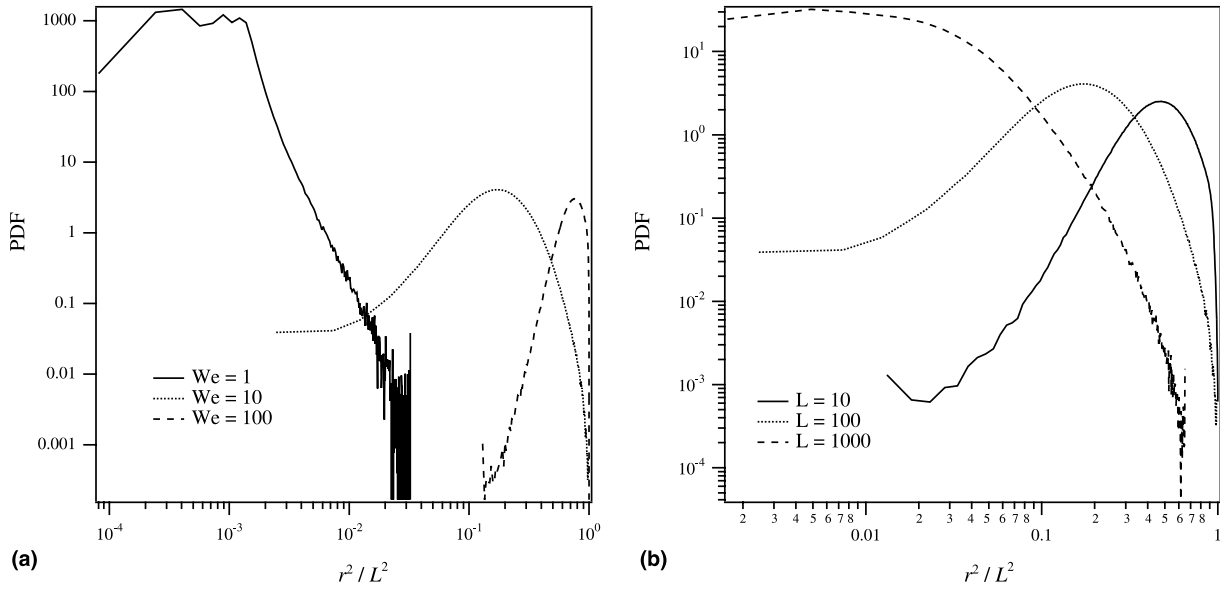

Fig. 2. PDF of r^2/L^2 for (a) the three values of Weissenberg number (see Runs 0–3 in Table 1) and (b) three values of maximum extension (see Runs 0, 1, 4 and 5 in Table 1).

(the mechanical energy is proportional to L^2). The effect of longer polymers can therefore be felt even at modest degrees of stretch.

Finally, we consider the effect of β on the turbulence in Runs 0, 2, and 4–8. Note that instead of varying β alone, we varied β and L simultaneously so as to keep fixed $(1-\beta)L^2$. The idea is based on the argument by Dimitropoulos et al. [10] that the important polymer parameter is the maximum extensional viscosity, which is proportional to $(1-\beta)L^2$. The results shown in Fig. 3 support this argument. In the cases we considered, there is consistent agreement between the two runs at different values of β, both in terms of the kinetic energy of the turbulence (see Table 1) and the PDF of the polymer extension. Indeed, the agreement is so good that it suggests a new scaling of the conformation tensor of the form

$$\mathbf{C}' \equiv \mathbf{C}/L^2. \tag{47}$$

The equation for $\mathbf{C}'$ would then take the form

$$\frac{\mathrm{D}\mathbf{C}'}{\mathrm{D}t} = \mathbf{C}'\cdot\nabla\mathbf{u} + \nabla\mathbf{u}^{\mathrm{T}}\cdot\mathbf{C}' - \frac{[f(r')\mathbf{C}' - \mathbf{I}/L^2]}{\tau_{\mathrm{p}}}, \tag{48}$$

where $r'^2 \equiv \mathrm{Tr}(\mathbf{C}')$ and

$$f(r') \equiv \frac{1-3/L^2}{1-r'^2}. \tag{49}$$

The polymer stress is then given by

$$\mathbf{T}^{[\mathrm{p}]} = \eta(1-\beta)L^2\underbrace{\frac{[f(r')\mathbf{C}' - \mathbf{I}/L^2]}{\tau_{\mathrm{p}}}}_{\Phi(We)}, \tag{50}$$

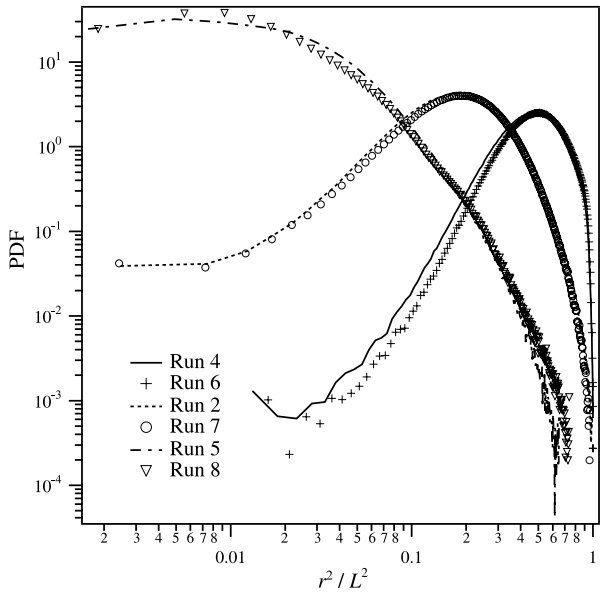

Fig. 3. PDF of the trace of **C** for the three values of Weissenberg number. The parameters correspond to Runs 0, 2 and 4–8 in Table 1.

where $\Phi(We)$ is the function above the bracket. Notice that for relatively long chained polymers (i.e., $L \gg 3$), the effect of L^2 on the evolution of $\mathbf{C}'$ or $\Phi(We)$ is relatively weak. This statement is not strictly true, since the terms proportional to L^{-2} are responsible for the polymer relaxing to its equilibrium state in the absence of flow. However, significant polymer stresses result from polymers far from equilibrium, in which these terms contribute negligibly; thus, the important contributions of $\mathbf{C}'$ to the fluid mechanics occur when polymers are stretched and $\mathbf{C}'$ is nearly independent of L. Under this assumption, the stress is determined by the product of a single lumped parameter $(1-\beta)L^2$ with the function $\Phi(We)$.

This has important implications for parameterizing drag reduction. It has long been known that longer-chain polymers can achieve drag reduction at lower concentrations [30]; however, the precise relationship between the two parameters was not known. According to the FENE-P model, the two parameters enter into the problem as a single combined variable, thus reducing the parameter space by one. It's important to see if such a reduction can be confirmed by experimental measurements, particularly across polymer types.

The decomposition also suggests a new way of thinking of the onset phenomenon. Empirically we know that below a critical Weissenberg number, polymers remain coiled and their effect on the flow is negligible (corresponding to $\Phi(We) \approx 0$). According to our reformulation of the FENE-P model, this is independent of β and L. In channel flow, the Weissenberg number increases with increasing Reynolds number until the threshold We^* is reached, whereupon polymer molecules undergo the coil–stretch transition. At this point, dictated only by We, we expect finite values of $\Phi(We)$. Further increases in the Reynolds number (and We) will cause $\Phi(We)$ to increase monotonically, indefinitely. The degree of drag reduction above criticality is then determined by the product of $\Phi(We)$ with the lumped parameter $(1-\beta)L^2$. Thus, onset is defined entirely in terms of a critical Weissenberg number We^*; there is no critical value for $(1-\beta)L^2$. However, practical considerations may limit the range of $(1-\beta)L^2$ for which drag reduction can be observed under typical experimental conditions.

Notice that the FENE-P model contains no critical polymer length parameter either. Deformation of the polymer in the model is based entirely on a local linear flow assumption and so the polymer length, relative

to the fluid mechanical length scales, is a small parameter that does not enter into the model. This implies there can be no critical length. (This is consistent with the most widely held view in the literature, see [31] for some discussion.) (see Fig. 3).

5.3. Decaying simulations

Decaying turbulence studies were carried out after forcing the system to a stationary state. Consequently, the polymer was pre-stretched, as would happen for example in a grid-generated system. Fig. 4 shows the turbulence intensity and mean square polymer extension as a function of time for a Newtonian fluid and for Weissenberg numbers of 10 and 100. We chose the two highest values because these yielded the largest effect. In both cases, we observe a form of 'drag reduction' at early times in which the polymer system decays more slowly than the Newtonian system. At later times it appears that the Newtonian and non-Newtonian systems both decay like a power law $t^{-\alpha}$, where the values of α are approximately the same. The early-time behavior is qualitatively similar to experimental observations by van Doorn et al. [32]. However, at longer times their measurements showed continued drag reduction, suggesting a self-similarity between the decay of energy and the decay of the polymer stretching. In our simulations, we see no such thing. In fact, this is not surprising with the FENE-P model. As the turbulent energy decays, the contribution of the polymer stresses will eventually become smaller than the Newtonian solvent stress, at which point the system reverts back to a Newtonian fluid. This is apparent in Fig. 4(b), which shows that r^2 approaches 3 (i.e., the equilibrium value) at long times.

Fig. 5 shows the effect of the polymer maximum extension, L, on the rate of decay of turbulent energy. Here we see the degree to which the polymer retards the rate of decay of turbulence increases with increasing L; however, at long times we again see that the decay rate of the polymer systems approach the Newtonian rate of decay. The explanation is essentially the same.

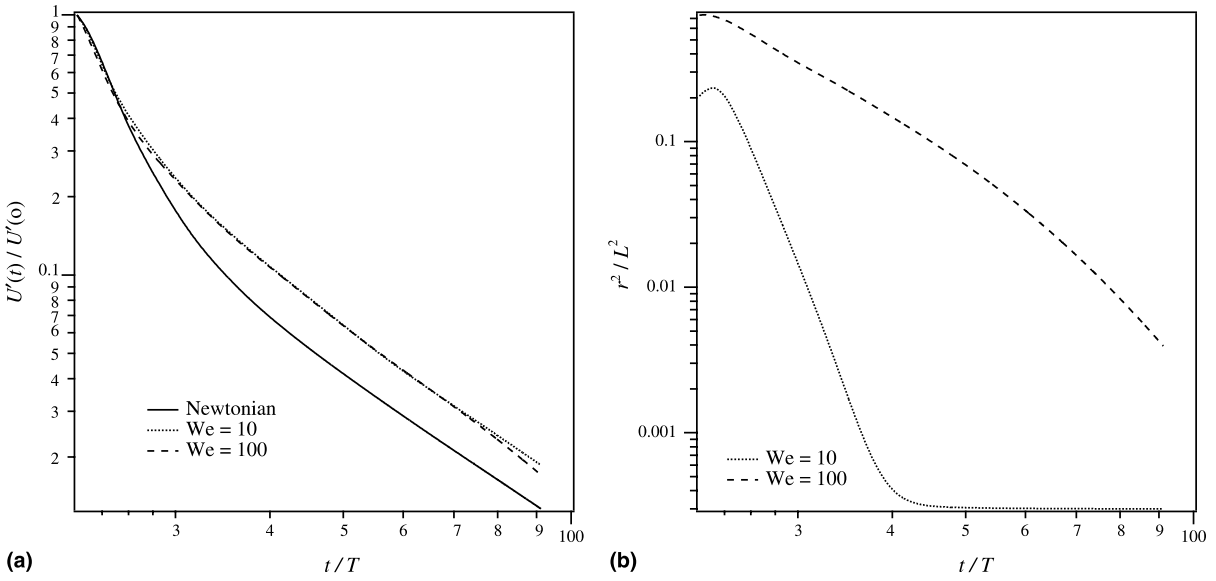

Fig. 4. (a) Normalized turbulence intensity as a function of time (normalized by the large eddy turnover time) for Runs 2 and 3, corresponding to the indicated Weissenberg numbers. (b) Equivalent plot of the normalized average square length of the polymer, $\overline{r^{r^2}} \equiv \overline{r^2}/L^2$, as a function of time.

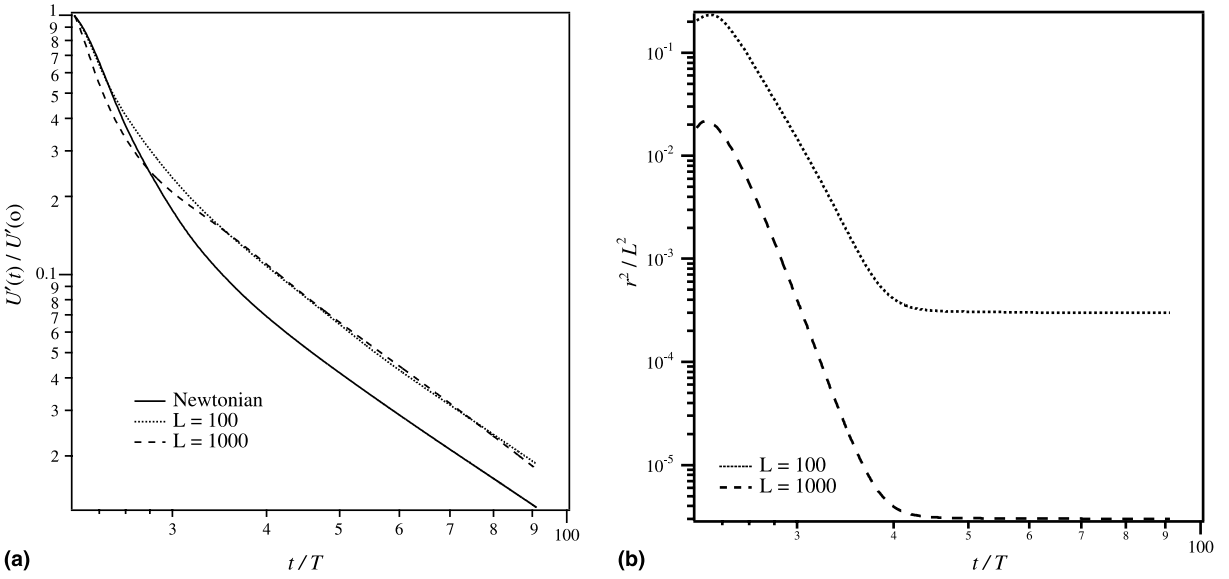

Fig. 5. (a) Normalized turbulence intensity as a function of time for Runs 2 and 5, corresponding to the indicated polymer maximum extensions. (b) Equivalent plot of the normalized average square length of the polymer, $\overline{r'^2} \equiv \overline{r^2}/L^2$, as a function of time.

5.4. Energy spectrum and grid resolution

Fig. 6 shows the Newtonian energy spectrum and three spectra corresponding to the *We* study and the *L* study. Notice in general the polymer spectra are slightly above the Newtonian spectrum at small wavenumbers, but are attenuated at intermediate wavenumbers. This low-wavenumber 'pivot' of the

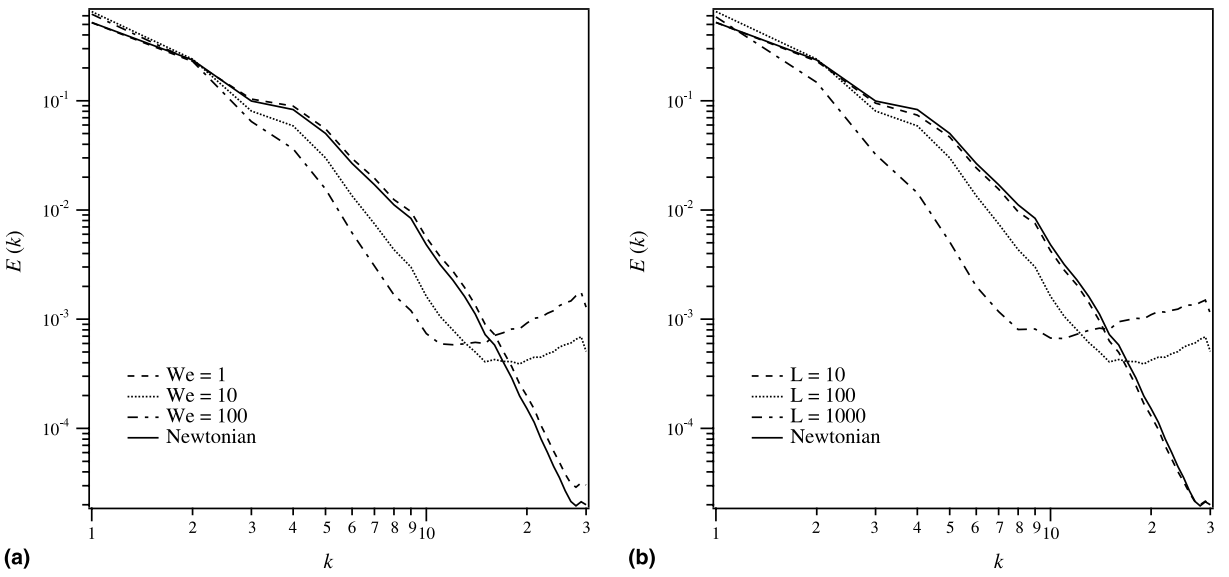

Fig. 6. Energy spectrum as a function of the (a) Weissenberg number ($L = 100$) and (b) maximum extension ($We = 10$).

spectrum is consistent with experimental observations in the literature [32,33]. We speculate that the attenuation at intermediate wavenumbers is due to polymer stretching, which consumes some of the mechanical energy.

What is less clear is whether the rise in the energy spectrum at high wavenumbers is real or an artifact of the model or numerical method. For example, this feature does not seem to be supported by experimental measurements. Moreover, numerical tests suggest that the source of this energy is the feedback from the large stress gradients that are generated by turbulent convection. This again raises the important question of numerical resolution of the conformation tensor **C** on a finite grid, in the absence of a stress diffusivity.

Dubief and Lele [15] discuss the analogy between the convection of **C** in the FENE-P model and advection of a passive scalar in the limit of vanishingly small diffusivity (i.e., $Sc \to \infty$). This is the limit considered by Batchelor [34], in which he derived the k^{-1} spectrum for $k > k_\eta \equiv (\epsilon/\nu^3)^{1/4}$. The spectrum arises from stretching and folding of the scalar down to finer and finer scales by Kolmogorov-scale eddies. This process is ultimately cut off by the molecular diffusivity if it exists. If we assume a similar stretching and folding process for **C** in the FENE-P model, then gradients of **C** (and correspondingly $\mathbf{T}^{[p]}$) will grow without bound.

This is unappealing on a number of levels beyond the obvious numerical resolution problems we noted earlier (see Fig. 1 and related discussion). For example, shocks in the **C** tensor will generate commensurately large gradients in the velocity field (indeed, this may be the cause of the tail in the energy spectrum we see in Fig. 6 at high wavenumbers).

Stress diffusivity. El-Kareh and Leal [35] recognized the potential for shocks to form in **C** due to its hyperbolic form. They argued that the standard FENE-P model is inconsistent in its treatment of relative motion of beads due to Brownian motion and the absolute motion of the entire molecule along its trajectory. Including the effect of Brownian motion of the whole molecule introduces a stress diffusivity into the equation for **C**, changing the character of the equation from hyperbolic to parabolic. From kinetic theory considerations, the estimate for the Schmidt number for a polymer molecule in a water-like solvent is in the range 10^5–10^6 [36]. While technically this eliminates the possibility of a discontinuity in **C**, it still allows for very large gradients to form. [2]

Sureshkumar and Beris [7] introduced a similar stress diffusivity into their numerical simulation of turbulent channel flow, but used a substantially lower value of the Schmidt number ($Sc = 0.8$). Their motivation was to suppress the formation of negative eigenvalues, which lead to the unbounded growth of instabilities. However, in light of the success we have had in eliminating negative eigenvalues through the Cholesky- and continuous eigendecompositions, it appears as though the more important role of the stress diffusivity may be to smooth out the shocks in **C**. Indeed, the value of Schmidt number they chose is more typical of numerical simulations of passive scalars [37], which, due to grid resolution requirements, rarely exceed a value of about 10 [38].

This raises two important questions. First, are the sub-Kolmogorov scale dynamics implied by $Sc \gg 1$ real? This is not at all certain, despite the apparent legitimacy of the scaling estimate $Sc \approx 10^5$ for Brownian polymer molecules. Experimental observations of the velocity spectrum do not show any evidence of the sub-Kolmogorov dynamics we observed in our simulations—in fact, they often show strong attenuation at high wavenumbers [32,33]. Furthermore, the simulations of Beris and co-workers are in apparent agreement with experimental measurements, despite the small Schmidt number they use. It seems at least plausible that some other mechanism is responsible for cutting off the steep gradients in **C**. We can think of two possibilities. First, the finite length of the stretched polymer chains may cause a breakdown of the local linear flow assumption used to derive the stretching terms in the FENE-P model. The Kolmogorov length

[2] The magnitude of the scalar gradient is proportional to the integral of k^2 times the spectrum, which scales like $Sc^{1/2}$ for $Sc \gg 1$, according to the Batchelor theory [34].

scale for a moderately high Reynolds number flow is of the order of 10 μm; given the typical radius of gyration of a polymer molecule in a good solvent (~50 nm), the linear flow assumption seems justified. However, the length of a stretched polymer chain can be 100 times its radius of gyration, making it the same order of magnitude as the Kolmogorov scale. This may limit the degree of stretching as well as the magnitude of gradients (in the direction of stretch). The second possibility is related to the low concentration of polymer in typical drag reducing flows. The large gradients in **C** result from continuous stretching and folding by turbulent convection, which at some point may not be sustainable due to the limited number of molecules.

The second question is if the sub-Kolmogorov motions exist, do they have any dynamical significance? It is possible that the sharp fronts in **C** are supported by high viscous stresses (velocity gradients) that are localized at small scales (high wavenumbers) and do not influence the large energetic scales very much. Under this circumstance, it may be justified to artificially lower the Schmidt number for numerical purposes.

In the absence of answers to these two important questions, we are left to speculate as to whether the high wavenumber behavior in Fig. 6 is real or artifact. It must be emphasized that answers should be sought *based on physical not numerical grounds*; once the physics is better understood, numerical algorithms that reproduce the known physics reliably can be developed. This is beyond the scope of the present study, which focused on the standard FENE-P model; however, we note that the Cholesky- and continuous eigendecompositions can be extended to include a stress diffusivity if that term is deemed necessary.

6. Conclusions

A numerical algorithm is presented for evolving the coupled FENE-P model for a dilute polymer solution with the Navier Stokes equations. The polymer stress in the FENE-P model is seen to involve a conformation tensor **C**, which is SPD by definition and must remain so to avoid spurious numerical instabilities. The approach is to decompose the matrix in one of two ways, evolve the components forward in time and construct the matrix from the components. In that way, the conformation tensor is guaranteed to be positive definite by construction. The new approach avoids many of the problems observed in earlier simulations of the equations, is robust, and expands the range of parameters that can be simulated, at least for the case of isotropic turbulent flow. (At the moment, we cannot say how effective the new algorithm will be for the more practical case of channel flow; we are in the process of developing a channel flow code based on this algorithm and we hope to compare that model to published results in the near future.)

The new algorithm has been implemented into an isotropic DNS code for the purposes of testing and to look at some physics of stirred and decaying turbulent polymer solutions. We are able to make calculations over the ranges $We \leqslant 100$ and $L \leqslant 1000$, which are realistic limits for these parameters. Our forced simulations show that the polymer expands and the turbulence is more attenuated with increasing We and L. From energy spectra, we see that turbulent energy in the intermediate scales is reduced (presumably because it is going into the polymer) while energy at high wavenumbers is increased by the presence of polymer. We conjecture that the traditional energy cascade in a Newtonian fluid is bifurcated into two directions: (i) the traditional triadic interactions leading to energy cascade; and (ii) into the polymer where energy is either reemitted at higher wavenumbers or dissipated into heat. The resulting net rate of energy transfer is reduced.

The decaying studies exhibited 'drag reduction' in the form of a reduction in the decay rate. This resulted from exchanges between the polymer potential energy and the turbulent kinetic energy that ultimately slows the overall decay rate in the system. It is difficult to compare 'drag reduction' in isotropic turbulence with the earlier work on channel flows, as the latter has many complications due to the presence of the wall. However, we can compare the scaling of the onset condition in the two flows. In pipe flow, the onset of drag reduction is usually defined in terms of a critical Weissenberg number based on wall variables

$$We_{\mathrm{W}} \equiv \frac{\tau_{\mathrm{p}}}{(\mu/\tau_{\mathrm{W}})},$$

where τ_{W} is the wall shear stress and the critical value for We_{W} is approximately 10 [9]. From energy considerations, we estimate the bulk ϵ to be

$$\epsilon = \frac{4\tau_{\mathrm{W}}\langle v\rangle}{\rho D},$$

where $\langle v\rangle$ is the mean velocity and D is the pipe diameter. Defining a critical Weissenberg number based on Kolmogorov variables yields the following estimate for the ratio of critical Weissenberg numbers

$$\frac{We_{\mathrm{W}}}{We} = \frac{\sqrt{fRe}}{2\sqrt{2}} \approx 0.01 Re^{3/8}, \tag{51}$$

where f is the Fanning friction factor, Re is the bulk Reynolds number, and we assume the Blasius relationship $f \approx 0.0791/Re^{1/4}$. Eq. (51) implies the two criteria are different; however, it is difficult to discern which is correct with the limited range of Reynolds numbers that can be simulated. For example, the above ratio is approximately 3 for $Re = 10,000$, which is numerically consistent with our DNS as well as most channel flow simulations.

Our new algorithms address the two numerical issues raised at the beginning of this article for the case of isotropic turbulence. However, the third important issue, namely convection of the conformation tensor, is not directly addressed by these algorithms. Instead, we have used our results to try and clarify the problem. The standard FENE-P model contains no diffusive process to cut off the sharp fronts that are formed in **C** by turbulent convection. This appears to be a limitation of the model (as opposed to the numerical algorithm) as we demonstrated by analogy with the passive scalar. The pathology here is even more important than for the passive scalar, as the sharp gradients ultimately lead to large accelerations in the fluid, which may or may not be real. Certainly if one takes this to the extreme limit (infinite resolution), the results seem inconsistent with most experimental observations. We have shown that the problem is not related to the loss of positive definiteness of **C**, as suggested in earlier publications, but is possibly related to the lack of a physical mechanism for smoothing the sharp fronts in **C**. Of course, other purely elastic instabilities that exist even in laminar flows may be causing some of the difficulties (see for example [39]). We hope these results will stimulate further work to clarify the physical origin of the molecular diffusive term (e.g., Brownian diffusion of polymer chains, finite length of chain, non-continuum effects) and better define its coefficient.

Acknowledgements

The authors thank Professor R.G. Larson for bringing to our attention [35,36] and for several helpful discussions on the limiting behavior of the FENE-P model. This research was supported by the DARPA Friction Drag Reduction Program Contract MDA972-01-C0032 and by the American Chemical Society Petroleum Research Fund Grant 36392-AC9.

References

[1] R.B. Bird, R.C. Armstrong, O. Hassager, Dynamics of Polymeric Liquids, vol. 1, second ed., Wiley, New York, 1987.
[2] R.G. Larson, H. Hu, D.E. Smith, S. Chu, Brownian dynamics simulations of a DNA molecule in an extensional flow field, J. Rheol. 43 (1999) 267–304.
[3] L. Li, R.G. Larson, T. Sridhar, Brownian dynamics simulations of dilute polystyrene solutions, J. Rheol. 44 (2000) 291.
[4] G.M. Harrison, J. Remmelgas, L.G. Leal, The dynamics of ultradilute polymer solutions in transient flow: comparison of dumbbell-based theory and experiment, J. Rheol. 42 (1998) 1039–1058.

[5] A. Peterlin, Streaming birefringence of soft linear macromolecules with finite chain length, Polymer 2 (1961) 257.
[6] F. Dupret, J.M. Marchal, Loss of evolution in the flow of viscoelastic fluids, J. Non-Newtonian Fluid Mech. 20 (1986) 143–171.
[7] R. Sureshkumar, A.N. Beris, Effect of artificial stress diffusivity on the stability of numerical calculations and the flow dynamics of time-dependent viscoelastic flows, J. Non-Newtonian Fluid Mech. 60 (1995) 53–80.
[8] A.N. Beris, R. Sureshkumar, Simulation of time-dependent viscoelastic channel Poiseuille flow at high reynolds numbers, Chem. Eng. Sci. 51 (1997) 1451–1471.
[9] R. Sureshkumar, A.N. Beris, R.A. Handler, Direct numerical simulation of turbulent channel flow of a polymer solution, Phys. Fluids 9 (1997) 743–755.
[10] C.D. Dimitropoulos, R. Sureshkumar, A.N. Beris, Direct numerical simulation of viscoelastic turbulent channel flow exhibiting drag reduction: effect of the variation of rheological parameters, J. Non-Newtonian Fluid Mech. 79 (1998) 433–468.
[11] C.D. Dimitropoulos, R. Sureshkumar, A.N. Beris, R.A. Handler, Budgets of Reynolds stress, kinetic energy and streamwise enstrophy in viscoelastic turbulent channel flow, Phys. Fluids 13 (2001) 1016–1027.
[12] B. Eckhardt, J. Kronjäger, J. Schumacher, Stretching of polymers in a turbulent environment, Comput. Phys. Commun. 147 (2002) 538–543.
[13] P. Ilg, E. de Angelis, I.V. Karlin, C.M. Casciola, S. Succi, Polymer dynamics in wall turbulent flow, Europhys. Lett. 58 (2002) 616–622.
[14] T. Min, J.Y. Yoo, H. Choi, Effect of spatial discretization schemes on numerical solutions of viscoelastic fluid flows, J. Non-Newtonian Fluid Mech. 100 (2001) 27–47.
[15] Y. Dubief, S.K. Lele, Direct numerical simulation of polymer flow, in: Center for Turbulence Research Annual Research Briefs, NASA Ames/Stanford University, 2001.
[16] J.M. Ottino, The Kinematics of Mixing: Stretching, Chaos and Transport, Cambridge University Press, Cambridge, 1989.
[17] R. Sureshkumar, A.N. Beris, Uniformly valid approximations for the conformational integrals resulting from Gaussian closure in the Hookean dumbbell model with internal viscosity, J. Rheol. 39 (1995) 1361–1384.
[18] V. Eswaran, S.B. Pope, An examination of forcing in direct numerical simulations of turbulence, Comput. Fluids 16 (1988) 257–278.
[19] J. Azaiez, G.M. Homsy, Numerical simulation of non-Newtonian free shear flows at high Reynolds numbers, J. Non-Newtonian Fluid Mech. 52 (1994) 333–374.
[20] A.N. Beris, B.J. Edwards, Thermodynamics of Flowing Systems With Internal Microstructure, Oxford University Press, New York, 1994.
[21] M.A. Hulsen, A sufficient condition for a positive definite configuration tensor in differential models, J. Non-Newtonian Fluid Mech. 38 (1990) 93–100.
[22] M. Lesieur, Turbulence in Fluids, Stochastic and Numerical Modeling, Nijhoff, Boston, 1987.
[23] G.S. Patterson, S.A. Orszag, Spectral calculation of isotropic turbulence: efficient removal of aliasing interactions, Phys. Fluids 14 (1971) 2538–2541.
[24] C. Zemach, The Handbook of Fluid Dynamics, Chapter Mathematics, CRC Press, Boca Raton, 1998.
[25] S.K. Lele, Compact finite difference schemes with spectral-like resolution, J. Comput. Phys. 103 (1991) 16–42.
[26] C. Canuto, M.Y. Hussaini, A. Quarteroni, T.A. Zang, Spectral Methods in Fluid Dynamics, Springer, New York, 1988.
[27] S. Sundaram, L.R. Collins, Collision statistics in an isotropic, particle-laden turbulent suspension I. direct numerical simulations, J. Fluid Mech. 335 (1997) 75–109.
[28] A. Iserles, Lie-group methods, Acta Numer. (2000) 215–365.
[29] E.G. Moody, L.R. Collins, Effect of mixing on nucleation and growth of titania particles, Aerosol Sci. Tech. (2002) (accepted).
[30] P.S. Virk, Drag reduction fundamentals, AIChE J. 21 (1975) 625–656.
[31] J.L. Lumley, Drag reduction in turbulent flow by polymer additives, J. Polymer Sci.: Macromolec. Rev. 7 (1973) 263–290.
[32] E. van Doorn, C.M. White, K.R. Sreenivasan, The decay of grid turbulence in polymer and surfactant solutions, Phys. Fluids 11 (1999) 2387–2393.
[33] M.D. Warholic, H. Massah, T.J. Hanratty, Influence of drag-reducing polymers on turbulence: effects of reynolds number, concentration and mixing, Exp. Fluids 27 (1999) 461–472.
[34] G.K. Batchelor, Small-scale variation of convected quantities like temperature in a turbulent fluid. Part 1. General discussion and the case of small conductivity, J. Fluid Mech. 5 (1959) 113–133.
[35] A.W. El-Kareh, L.G. Leal, Existence of solutions for all Deborah numbers for a non-Newtonian model modified to include diffusion, J. Non-Newtonian Fluid Mech. 33 (1989) 257–287.
[36] A.V. Bhave, R.B. Armstrong, R.A. Brown, Kinetic theory and rheology of dilute, nonhomogeneous polymer solutions, J. Chem. Phys. 95 (1991) 2988–3000.
[37] S. Herr, L.-P. Wang, L.R. Collins, EDQNM model of a passive scalar with a uniform mean gradient, Phys. Fluids 8 (1996) 1588–1608.
[38] D. Bogucki, J.A. Domaradzki, P.-K. Yeung, Direct numerical simulations of passive scalars with $Pr > 1$ advected by turbulent flow, J. Fluid Mech. 343 (1997) 111–130.
[39] E.S.G. Shaqfeh, Fully elastic instabilities in viscometric flows, Annu. Rev. Fluid Mech. 28 (1996) 129–185.